Structure and Dynamics of the Actin Filament†

Jing-Qu Guan,[‡,§] Keiji Takamoto,[‡,§] Steven C. Almo,[‡,||] Emil Reisler,[⊥,#] and Mark R. Chance*[,‡,§,||]

Center for Synchrotron Biosciences, Department of Physiology and Biophysics, and Department of Biochemistry, Albert Einstein College of Medicine of Yeshiva University, 1300 Morris Park Avenue, Bronx, New York 10461, and Department of Chemistry and Biochemistry and the Molecular Biology Institute, University of California, Los Angeles, California 90024

Received September 14, 2004; Revised Manuscript Received December 13, 2004

ABSTRACT: The structures of filamentous Mg-ATP-actin (F actin) in the presence and absence of KCl have been mapped with hydroxyl radicals (·OH) generated by synchrotron X-ray radiolysis. Proteolysis and mass spectrometry (MS) analysis revealed 52 reactive side-chain sites from 27 distinct peptides within actin. The reactivities of these probe sites with ·OH in the F-actin states are compared with those of Mg-ATP-G-actin (monomers) analyzed previously [Guan, J.-Q. et al. (2003) *Biochemistry 42*, 11992−12000]. Filament-dependent protection within subdomains 2, 3, and 4 and at the C terminus is consistent with longitudinal contacts of monomers within the filament helical structure as predicted by the Holmes model. In the absence of KCl, the extent of filament-dependent protection rarely reached 3-fold, consistent with a highly dynamic filament characterized by relatively weak interactions between actin protomers. However, in the presence of KCl, the extents of protection are significantly increased, consistent with a well-ordered, more tightly packed filament structure. Filament-dependent enhancements of reactivity not predicted by the Holmes model are seen for a peptide that overlaps the "hydrophobic plug" (H-plug) region and for a peptide that forms contacts with the polyphosphate moiety of the bound nucleotide. Overall, these data are both consistent with and complementary to a recent deuterium-exchange MS study of filamentous actin [Chik, J. K., and Schriemer, D.C. (2003) *J. Mol. Biol*. *334*, 373−385], which also did not detect any burial of the H plug upon formation of filaments.

The temporal and spatial regulation of actin-filament assembly is central to the control of important cellular processes such as cytokinesis, endocytosis, and overall cell motility. Numerous actin-binding proteins serve to mediate the interconversion of actin monomers (G actin)[1] and its filamentous state (F actin) under the influence of a variety of signal transduction pathways (*1*−*3*). An understanding of these processes requires detailed structural models for actin in both its monomeric and filamentous states. High-resolution structures of adenosine 5′-triphosphate (ATP) and ADP actin (covalently modified at Cys-374) are available (*4*, *5*), and the structure of actin monomers has also been analyzed in their complexes with various actin-binding proteins (*6*−*11*). Actin possesses a small domain composed of subdomains 1 and 2 and a large domain composed of subdomains 3 and 4. Divalent-cation-associated ATP is bound deep within the cleft formed by the large and small domains. Actin-binding proteins such as DNase I bind to the highly flexible "D loop" on subdomain 2, while gelsolin segment-1 and profilin bind in the cleft formed between subdomains 1 and 3. A helical model for the structure of the actin filament has been generated by fitting the atomic structure of the rabbit skeletal muscle actin monomer (*6*) to 8 Å resolution X-ray fiber diffraction data (*12*, *13*). The resulting model, shown in Figure 1, may be described as that of two parallel strands of actin protomers that twist around one another to form an actin helix. Within the model, residues 322−325 of subdomain 3 of one monomer make longitudinal contacts with residues 243−245 in subdomain 4 of a second monomer, while residues 286−289 in subdomain 3 longitudinally interact with residues 202−204 in subdomain 4. In addition, residues 166−169 in subdomain 3 and residue 375 in subdomain 1 make longitudinal contacts with residues 41−45 within the DNase-I-binding loop (D loop) of subdomain 2. Lateral contacts between the filament strands are proposed to be mediated by a hydrophobic "plug" (the H loop) composed of residues 264−273.

The structures of both F and G actins are quite sensitive to solution conditions including monovalent and divalent cation binding and the phosphorylation state of bound

† This research is supported in part by the National Institute for Biomedical Imaging and Bioengineering under the Biotechnology Centers program (P41-EB-01979 to M.R.C.), by USPHS R01-GM-53807 (to S.C.A.) and USPHS RO1-AR-20231 and NSF MCB 0316269 (to E.R.).

* To whom correspondence should be addressed: Department of Physiology and Biophysics, Albert Einstein College of Medicine, 1300 Morris Park Avenue, Bronx, NY 10461. Telephone: (718) 430-4136. Fax: (718) 430-8587. E-mail: mrc@aecom.yu.edu.

‡ Center for Synchrotron Biosciences, Albert Einstein College of Medicine of Yeshiva University.

§ Department of Physiology and Biophysics, Albert Einstein College of Medicine of Yeshiva University.

|| Department of Biochemistry, Albert Einstein College of Medicine of Yeshiva University.

⊥ Department of Chemistry and Biochemistry, University of California.

Molecular Biology Institute, University of California.

[1] Abbreviations: ATP, adenosine 5′-triphosphate; EGTA, ethylene glycol-bis(2-aminoethyl ether)-*N*,*N*,*N*′,*N*′-tetraacetic acid; EM, electron microscopy; G actin, monomeric actin; F actin, filamentous actin; DTT, dithiothreitol; TFA, trifluoroacetic acid; HPLC, high-performance liquid chromatography; MS, mass spectrometry; ESI, electronspray ionization; DLS, dynamic light scattering.

10.1021/bi048021j CCC: $30.25
Published on Web 02/10/2005

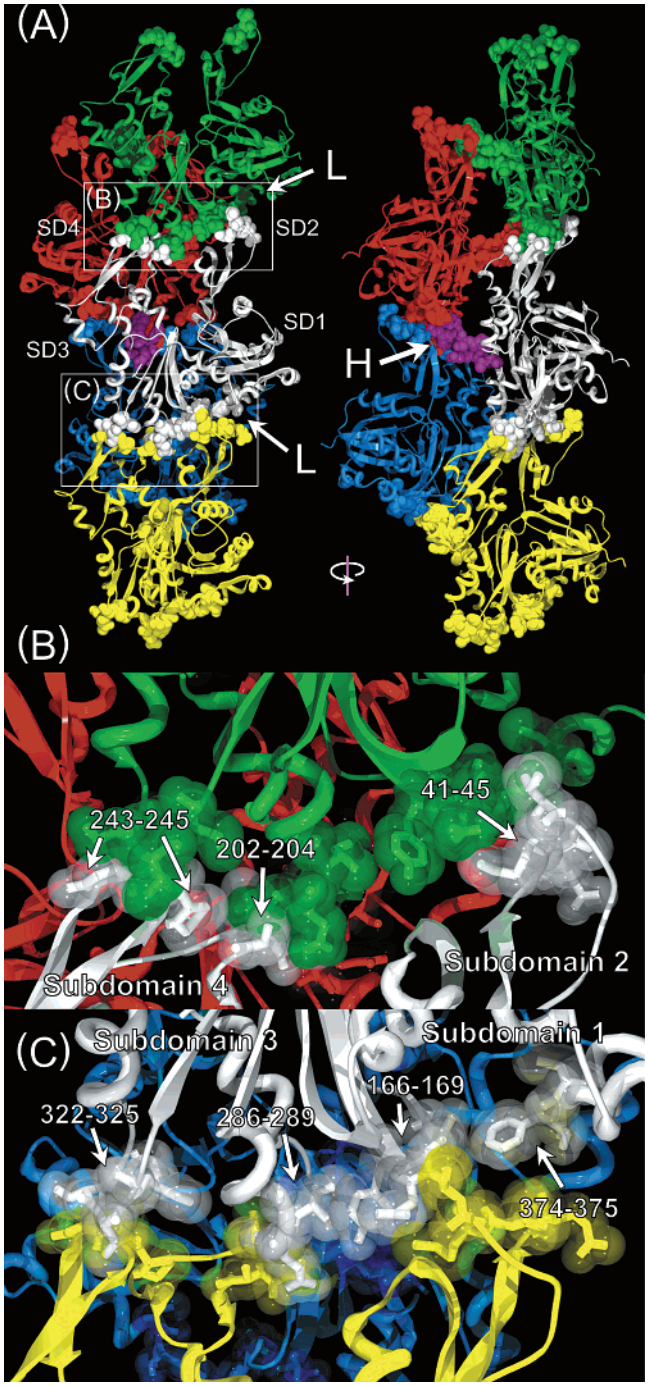

FIGURE 1: Actin-filament structure. The structure shown in this figure is from the Holmes model (*12*). (A) Structure of helical model composed of 5 monomers. The interactions predicted in the model are shown as "space-fill" representations in the structure. The H plug of the white-colored monomer is colored purple for clarity. In A, "H" and "L" indicate H plug and longitudinal interactions, respectively. (B) Magnified view of the white-boxed region (B) in A. The residues 41−45 in subdomain 2 and residues 202−204 and 243−245 are predicted to interact with the green monomer and expected to be protected in F actin. The residue numbers indicated in B are for the white monomer. (C) Magnified view of the white-boxed region (C) in A. Same as in B, all residue numbers are for the white monomer. Four sites are expected to be protected in subdomains 1 and 3.

nucleotide. In particular, the state of bound nucleotide is thought to provide structural signals mediating the binding of specific actin-binding proteins to regulate filament assembly and disassembly (*1*, *2*, *14*). Synchrotron radiolysis and mass spectrometry (MS) are effective and attractive approaches to examine the structural and dynamic features of filamentous actin and associated complexes, because many of these functional states are refractory to analysis by crystallography or NMR methods (*15*, *16*). In our protein footprinting approach, hydroxyl radicals are generated from millisecond exposure of aqueous solutions to unattenuated "white" synchrotron radiation resulting in stable oxidative modifications of solvent-accessible and reactive amino acid side chains. The specific extents and sites of oxidative modification are quantified after proteolytic digestion using liquid chromatography (LC)−MS and LC−MS/MS methods (*15*−*21*). The analytical approach is similar to deuterium-exchange MS surface-accessibility mapping (*22*, *23*); however, radiolysis preferentially modifies specific, reactive side chains, while deuterium exchange probes peptide segments and interrogates the susceptibility of the backbone to exchange. Deuteration kinetics depends on both conformational stability of the protein secondary structure as well as surface accessibility (*24*, *25*), while the radiolytic footprinting approach primarily provides a quantitative measure of the time or population average solvent accessibility of the probe residues.

We have previously used radiolytic footprinting to define the structural differences between Mg-ATP and Ca-ATP actin monomers (*15*, *16*). The results suggest reduced solvent accessibility of the cleft between subdomains 2 and 4 and a C terminus more closely packed against subdomain 1 for Mg-ATP-G-actin. This structural change may be associated with the lower critical concentration observed for the formation of filaments in the case of Mg-ATP actin monomers. Deuterium-exchange MS experiment have also been carried out on Ca-ATP G and F actins (*25*); the decreases in deuteration of peptides derived from filamentous preparations compared to monomers provide support for the helical model of actin (*12*). In this work, we examine the surface-accessible and reactive side-chain residues of Mg-ATP-actin filaments in the presence and absence of 50 mM KCl. Consistent with the picture derived from deuterium-exchange MS data, filaments prepared in the presence of KCl exhibit protections (as compared to actin monomers) that are largely consistent with a regular helical structure.

EXPERIMENTAL PROCEDURES

Protein Purification. Rabbit skeleton actin (Ca-G-actin) was prepared as described by Spudich and Watt (*26*) and stored at 4 °C in Ca-G-buffer (2 mM Tris at pH 7.6, 0.2 mM ATP, 0.5 mM dithiothreitol (DTT), 0.2 mM $CaCl_2$, and 1 mM NaN_3), which was freshly prepared and exchanged daily. Mg-F-actin was prepared by adding $MgCl_2$ and ethylene glycol-bis(2-aminoethyl ether)-*N*,*N*,*N*′,*N*′-tetraacetic acid (EGTA) (final concentrations, 2 mM $MgCl_2$ and 1 mM EGTA) to a solution of Ca-G-actin at 15 μM in Ca-G-buffer, followed by an incubation at 4 °C for 30 min, and dialyzed against Mg-F-buffer (2 mM Tris at pH 7.6, 0.2 mM ATP, 0.5 mM DTT, 0.2 mM $MgCl_2$, and 1 mM NaN_3) for 3 days before any use. During this time, the Mg-F-buffer was also freshly prepared and exchanged daily. Mg-KCl-F-actin was prepared by using the same procedures as Mg-F-actin, except that KCl (50 mM) was present in solution.

Synchrotron X-ray Radiolysis. Prior to radiolysis experiments, Ca-G-actin (15 μM), Mg-F-actin (15 μM), and Mg-

KCl-F-actin (15 μM) were dialyzed against Ca-G-actin radiolysis buffer (2 mM sodium cacodylate at pH 7.6, 0.2 mM $CaCl_2$, and 0.2 mM ATP), Mg-F-actin radiolysis buffer (2 mM sodium cacodylate at pH 7.6, 0.2 mM $MgCl_2$, and 0.2 mM ATP), and Mg-KCl-F-actin radiolysis buffer (2 mM sodium cacodylate at pH 7.6, KCl 50 mM, 0.2 mM $MgCl_2$, and 0.2 mM ATP), respectively. All synchrotron-exposure experiments were performed at the X-28C beamline of the National Synchrotron Light Source (NSLS), Brookhaven National Laboratory. Exposure times were controlled by using an electronic shutter (Vincent Associates) and ranged from 0 to 200 ms. The storage ring energy was 2.8 GeV, and ring currents ranged from 136 to 289 mA throughout all of the experiments in this study (*16*, *18*, *21*).

Electron Microscopy (EM). Actin samples were transferred to grids and negatively stained with 1% phosphotungstic acid at 4 °C. The grids were then blotted dry before immediate observation in a JEOL 100CX II transmission electron microscope (JEOL USA, Inc.) at 80 kV.

Dynamic Light Scattering (DLS). All DLS measurements were acquired by using a DynaPro MS/X dynamic light-scattering instrument (Protein Solutions, Charlottesville, VA) at 4 °C. Prior to the DLS experiments, NaN_3 and DTT in G actin, Mg-F-actin, and Mg-KCl-F-actin samples were removed by dialysis against Ca-G-actin radiolysis buffer, Mg-F-actin radiolysis buffer, and Mg-KCl-F-actin radiolysis buffer, respectively. Three independent data sets were collected by the DynoPro Instrument Control Software, version 5.26. The time-dependent autocorrelation function of the photocurrent was acquired every 10 s, with 10 acquisitions for each run. The sample protein solution in a "Uvette" cuvette (160−1600 nm cutoff, Eppendorf) was illuminated by an 824.6 nm laser, and the intensity of light scattered at an angle of 90° was measured by a solid-state avalanche photodiode.

Mass Spectrometric Analysis (MS and MS/MS). Radiolyzed samples were denatured in acetonitrile prior to proteolysis with sequencing-grade modified trypsin, endoproteinase Asp-N, and endoproteinase Glu-C (Roche). After enzymatic proteolysis, the resulting peptide mixtures were separated and analyzed using a coupled high-performance liquid chromatography (HPLC)−electrospray ionization (ESI)−MS LCQ system (ThermoFinnigan). Reverse-phase HPLC was performed on a Waters 2690 Separations Module (Waters Corporation), using a C18 (Vydac) 1.0 × 150 mm column for all digested protein samples. Buffer A [95% water, 5% acetonitrile, and 0.06% trifluoroacetic acid (TFA)] and buffer B (90% acetonitrile, 10% water, and 0.055% TFA) were used to establish a gradient. The HPLC elute was directed to a Finnigan LCQ quardrupole ion trap mass spectrometer with a needle voltage of 4.5 kV. The samples were scanned for 60−75 min, and the spectra were acquired in the positive-ion mode for masses corresponding to an *m*/*z* range of 400−2000. The sites of oxidative modification were determined by tandem HPLC−MS/MS. For the acquisition of MS/MS data, a 1.0 unit *m*/*z* range was used in selecting the parent ion for fragmentation in the second stage of the mass spectrometer (*17*, *21*).

Calculation of Solvent-Accessible Surface Areas (ASAs). ASA calculations of the Holmes model of actin including the nucleotide were carried out using the GETAREA server (http://www.scsb.utmb.edu/cgi-bin/get_a_form.tcl) with a modified residue type library for ADP and ATP defined. The coordinates used were obtained from the following server (FTP 149.217.48.3). The model structure was truncated to a structure composed of five monomers, in which the third monomer has all of the relevant interactions with neighboring monomers. A single monomer was also taken from the model and was subjected to the ASA calculations. The ASAs for the third monomer in the five-monomer model and the isolated third monomer were compared and also related to the 1ATN crystal structure with DNase I removed (*6*).

Visualization of 3D Structures. The coordinates are visualized using Swiss PDB Viewer version 3.7, and POV-Ray 3 scenes were generated. Rendering of images was accomplished using POV-Ray 3.5 under both Windows 2000 and Linux (RedHat 9), after scene parameters were manually manipulated.

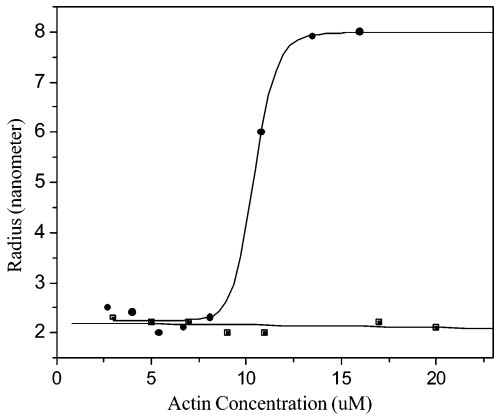

FIGURE 2: DLS data of Ca and Mg actin as a function of the concentration at low salt. The calculated hydrodynamic radius (in nanometers) is plotted versus the actin concentration (in micromolars). A highly cooperative transition with a midpoint of 10 μM (see the text) indicative of filament formation is seen for the Mg-actin species, while the Ca-actin species shows no significant changes. Mg-ATP-actin (●) and Ca-ATP-actin (■).

RESULTS

Oligomerization States of Actin. We examined the polymerization behavior of actin preparations using DLS and EM. Figure 2 shows DLS data for Ca and Mg actin as a function of the actin concentration. Over the concentration range examined, Ca actin experiences no significant changes in the observed particle radius; it behaves as a monomer throughout the experiment. However, Mg actin experiences a highly cooperative transition where it apparently changes from a monomeric to an oligomeric state with a midpoint of 10 ± 1 μM actin (*27*). Preparations of Mg actin in 50 mM KCl show a radius indicative of F actin at concentrations from 2.5 to 25 μM (data not shown). EM analysis of the filaments in the absence of KCl (Figure 3) reveals extended filaments of lengths of thousands of monomer units with an average width of 7 ± 1 nm, similar to previous results (*14*). Analysis of EM pictures of the KCl oligomers gave similar results (data not shown). Overall, these data confirm the structural parameters for the monomers and filaments studied in this paper and define the solution conditions under which they interconvert.

Oxidation Rates as a Function of the Protein Concentration. On the basis of the above findings, we designed experiments to analyze the oligomerization-dependent pro-

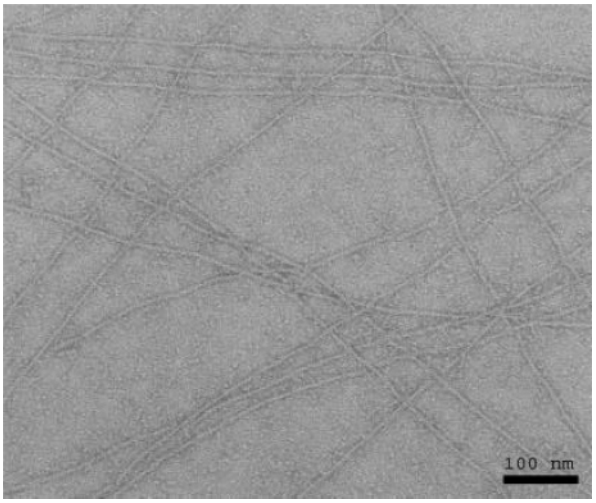

FIGURE 3: Electron microscope pictures of the negatively stained filaments in the absence of KCl. Extended filaments with averaged widths of 7 ± 1 nm are observed. Analysis of filaments in the presence of KCl yielded similar results.

tections for Mg monomers. Previously, we had established that a 5 μM actin concentration provided a homogeneous population of Mg monomers in the absence of KCl [Figure 2 (*16*)]. The oligomeric state is >95% occupied at 15 μM actin; thus, we chose this as the actin concentration for examining the filamentous state, both in the presence and absence of KCl. Given these conditions, we subsequently designed a set of experiments such that protein concentration-dependent changes in side-chain reactivity could be distinguished from changes in reactivity because of conformational changes. For example, for two footprinting experiments at different concentrations of protein (where no changes in the conformation of the protein occur), we expect lower overall reactivity as the protein concentration increases, because the dose of hydroxyl radicals will be distributed over a higher effective concentration of target sites (*28*). However, this phenomenon is not strictly linear; hydroxyl radical self-reaction (forming peroxide) is concentration-dependent and competes with the reactions that oxidize protein targets (*28*, *29*). Thus, we expect that if we compare the side-chain reactivity of Mg actin at 5 and 15 μM concentrations, the results will be complicated by protein concentration-dependent changes as well as changes because of oligomerization. To distinguish these effects, we examined the reactivity of peptides within Ca actin at 5 and 15 μM, because Ca actin has no apparent change in conformation over this concentration range (Figure 2).

Actin was digested using trypsin, Asp-N, and Glu-C to produce a set of peptides that covers 80−85% of the protein sequence. The N terminus was identified as acetylated and His-73, as methylated, as shown previously (*16*). Modification rate constants for all monitored peptides are shown in Table 1. The first three columns show the sequence range, protease, and subdomain location of the peptides examined. The previously reported oxidation rate constants for Ca actin at 5 μM are shown in column 4 (*16*). Column 5 shows the rate constants for peptides derived from Ca actin at 15 μM concentration that were examined in this study. In column 6, we calculate the percentage reduction in modification rate for 15 μM Ca-actin samples compared to Ca-actin samples examined at 5 μM. It can be seen in virtually every case that the apparent rate is decreased as the protein concentration

Table 1: Oxidation Rates of Peptides in Actins in Different States from Proteolysis with Tryspin, Asp-N, and Glu-C[a]

peptide	protease	subdomain	Ca-G-actin (5 μM)	Ca-G-actin (15 μM)	reduction (%)	Mg-G-actin (5 μM)	Mg-G-actin (15 μM)	Mg-F-actin (15 μM)	Mg-KCl-F-actin (15 μM)
1−18	trypsin	1	7.3	5.6	23	6.1	5.3	2.6	2.4
19−28		1	0.65	0.72	−11	0.32	0.28	0.1	0.02
40−50		2	33	25	24	20	17.5	13	1.7
51−61		2	0.69	0.56	19	0.32	0.28	0.14	0.08
63−68		2	0.4	0.35	12	0.08	0.07	0.04	0.04
69−84		1 and 2	7.3	6.5	11	5.5	4.8	2.2	1.4
85−95		1	2.8	2.4	14	2.9	2.5	2.6	0.31
96−113		1	0.5	0.48	4	0.52	0.45	0.19	0.17
119−147		1 and 3	14	13	7	12	10.5	4	0.84
184−191		4	10	8	20	10	8.8	5	4.9
197−206		4	0.83	0.73	12	0.24	0.21	0.2	0.13
239−254		4	0.75	0.76	−1.3	0.3	0.26	0.27	0.11
292−312		3	14	8.9	36	11	10	7.3	6.1
316−326		3	8.2	6.6	20	6.1	5.3	6.3	3
329−335		3	0.78	0.75	3.8	0.72	0.63	0.78	0.62
360−372		1	0.72	0.72	0	0.38	0.33	0.41	0.17
11−23	AspN	2	0.7	0.65	7	0.43	0.38	0.122	0.08
157−178		3	9.8	9.5	3	12	10.5	17	36
222−243		4	7.7	7.6	1.3	6.5	5.7	7	4.4
292−310		3	12	9	25	12	10.5	8.2	6.7
363−375		1	8.5	6.8	20	3.6	3.1	1.1	0.57
58−72	GluC	2	1.1	0.96	13	0.18	0.16	0.15	0.08
84−93		1	2.9	2.7	7	2.8	2.4	2.5	0.65
118−125		1	8.4	7.1	15	7.3	6.4	3.3	0.81
196−207		4	1.1	0.88	20	0.26	0.23	0.24	0.15
242−253		4	0.69	0.65	6	0.26	0.23	0.3	0.23
260−270		4	7.9	6.8	14	8.8	7.7	32	31

[a] Columns 1−3 are the sequence, protease, and subdomain location, respectively. Column 4, Ca-G-actin at 5 M; column 5, Ca-G-actin at 15 M; column 6, average reduction in the rate of column 4 versus column 5; column 7, Mg-G-actin at 5 M; column 8, calculated Mg-G-actin rate expected for 15 M; column 9, Mg-F-actin at 15 M; and column 10, Mg-KCl-F-actin at 15 M. The data for Mg-G-actin at 15 M (column 8) were obtained by applying the average percentage reduction seen in column 6 (see the text).

Table 2: Ratios of Rates for the Effective Mg Monomer Divided by the Rates for the Mg Oligomer in the Absence (Column 4) and Presence (Column 5) of KCl[a]

peptide	oxidized residues	subdomain	Mg-G-actin (15 μM)/ Mg-F-actin (15 μM)	Mg-G-actin (15 μM)/ Mg-F-KCl-actin (15 μM)
1−18	10C, 16L	1	2.0	2.2
19−28	21F	1	2.8	14.0
40−50	40H, 44M, 47M	2	1.3	10.3
51−61	53Y	2	2.0	3.5
63−68	67L	2	1.8	1.8
69−84	69Y, 73H, 79W, 82M	1 and 2 (69)	2.2	3.4
85−95	87H, 88H, 90F, 91Y	1	1.0	8.1
96−113	101H, 102P, 110L, 112P	1	2.4	2.6
119−147	119M, 123M, 124F, 143Y	1 and 3 (143)	2.6	12.5
184−191	190M	4	1.8	1.8
197−206	200F−202T	4	1.1	1.6
239−254	243P	4	1.0	2.4
292−312	305M−307P	3	1.4	1.6
316−326	322P, 325M	3	0.8	1.8
329−335	332P, 333P	3	0.8	1.0
360−372	362Y, 367P, 371H	1	0.8	1.9
11−23	21F	2	3.1	4.8
157−178	161H, 164P, 166Y, 169Y, 171L−173H, 176M	3	0.6	0.3
222−243	227M, 236L, 243P	4	0.8	1.3
292−310	305M−307P	3	1.3	1.6
363−375	367P, 371H, 374C, 375F	1	2.8	5.4
58−72	67L, 69Y	2	1.1	2.0
84−93	87H, 88H, 90F, 91Y	1	1.0	3.7
118−125	119M, 123M, 124F	1	1.9	7.9
196−207	200F−202T	4	1.0	1.5
242−253	243P	4	0.8	*b*
260−270	269M	4	0.2	0.2

[a] The rates for each peptide in Mg-G-actin, Mg-F-actin, and Mg-KCl-F-actin from Table 1 were used to calculate these ratios. Listed in columns 2 and 3 are the oxidized residues in each peptide (sequence numbers listed in column 1) and their locations in actin subdomains, respectively.[b] Data cannot be accurately determined.

increases; the average reduction for the 26 peptides is 12% (±10) (column 6). This represents the concentration-dependent suppression effect for the 3-fold change in actin concentration from 5 to 15 μM. Column 7 shows the oxidation rates for the 26 Mg-G actin peptides at 5 μM reported previously (*16*). To normalize these data to represent the expected rate of reactivity for Mg-G actin species at 15 μM concentration, we apply the average reduction in rate of 12% to each of the values in column 7 to generate the data of column 8. We used the average observed reduction to normalize the rate data instead of the individual peptide by peptide values because the latter had significant variations. These variations are to be expected because of propagation of errors in the division of small numbers. Columns 9 and 10 show the oxidation rate data for the Mg-ATP filament preparations of this study in the absence and presence of KCl, respectively.

Filament-Dependent Protections in the Actin Structure. Table 2 presents the oxidation rate data for Mg filaments in both the presence and absence of KCl as ratios of rates for the effective Mg monomer divided by the rates for the Mg oligomer. Thus, values greater than 1.0 indicate filament-dependent decreases in reactivity (or protections), while values less than 1.0 indicate enhancements of reactivity because of filament formation. On the basis of our previous footprinting data (*11*, *15*−*21*), the use of a normalization to provide the numerator rate in the ratio, and in consideration of the overall experimental errors, we adopt a conservative standard that ratios between 0.8 and 1.2 should be considered to represent no change in reactivity. Values of 0.7 or less are judged to be reliable indicators of reactivity enhancement, and values of 1.3 or greater represent protection.

Filament-dependent protection is observed in many of the peptides examined in the absence of KCl. A total of 14 of the 26 peptides showed protection, including peptides composed of residues 1−18, 19−28, 40−50, 51−61, 63−68, 69−84, 96−113, 119−147, 184−191, and 292−312 from trypsin digests; 11−23, 292−310, and 363−375 from Asp-N digests; and 118−125 from Glu-C digests. The specific residues that represent the structural probes for the experiments as determined by tandem MS are shown in Table 2 (*16*) and are illustrated on the structure of the actin monomer in Figures 4 and 5.

Within subdomain 2, His-40, Met-44, and Met-47 within the D loop, Leu-67, and Tyr-69 within the nucleotide cleft as well as Tyr-53 and His-73 experience protection as a function of oligomerization (Figure 4). Our previous footprinting results on the divalent-cation-dependent changes in the actin monomer structure indicated Mg-dependent protection of residues on both sides of the cleft between subdomains 2 and 4; increases in protection for Leu-67 and Tyr-69 indicate that the cleft is increasingly inaccessible in the Mg-dependent filament.

Residues within subdomain 3, such as Met-305, Tyr-306, and Pro-307 from peptides 292−312 (trypsin) and 292−310 (Asp-N), show filament-dependent protections, while multiple residues within peptide 157−178 in subdomain 3 show filament-dependent enhancements in reactivity (colored blue in Figure 4). Only one other peptide, from residues 260−270 in subdomain 4, shows such an enhancement.

Residues within subdomain 1, such as Cys-10, Leu-16, and Phe-21, along with multiple residues from peptides 96−113 and 119−147 (the latter confirmed by data from peptide 118−125), such as His-101, Pro-102, Leu-110, Pro-112, Met-

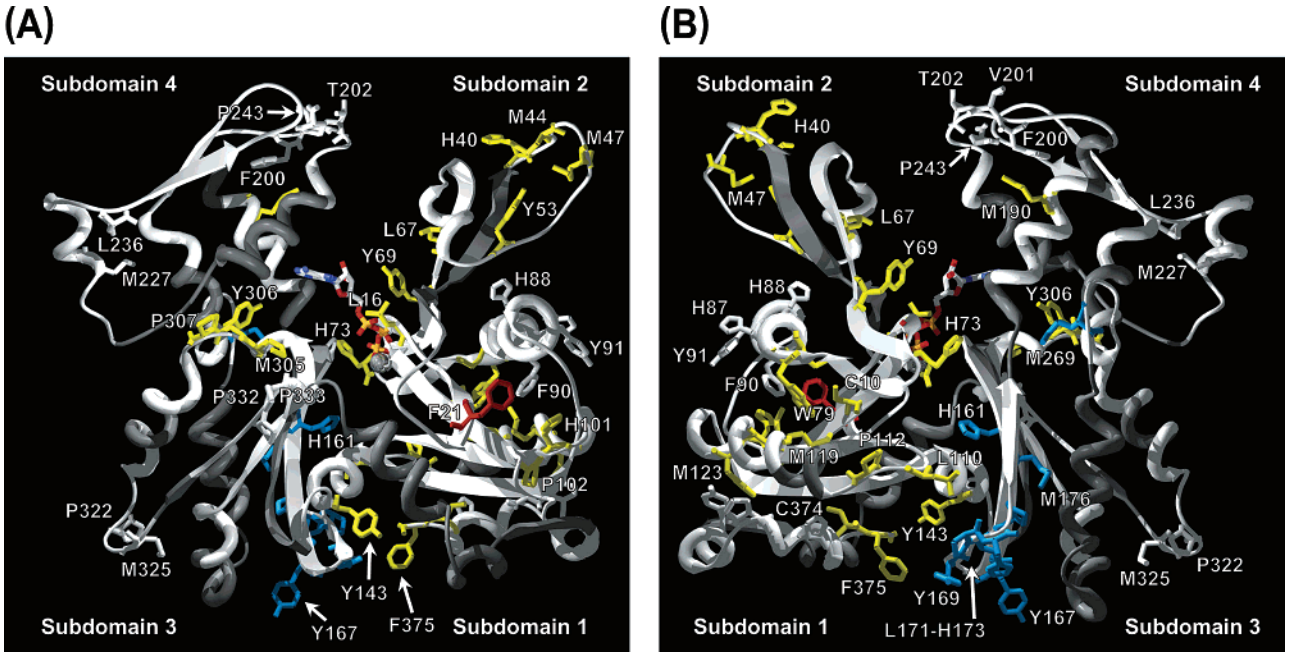

FIGURE 4: Protection sites observed in Mg-F-actin without KCl revealed by hydroxyl radical footprinting as mapped on the crystal structure 1ATN (with DNase I removed). (A) Front view. (B) Backside view (180° rotation from A). The side chains of the probe residues are colored (and labeled for identification) according to the protection ratios from Table 2. Side chains are colored white for protection ratios from 0.8 to 1.2 (e.g., no change within error). Yellow-colored side chains indicate moderate protection as a function of filament formation (from 1.3 to 2.9), and red-colored side chains indicate robust protections (beyond 2.9). The blue-colored side chains indicate residues that experience enhanced modification rates in F actin (protection ratio < 0.8). The regions with a gray backbone indicate peptides that are not observed in this study, while the observed peptides are colored white.

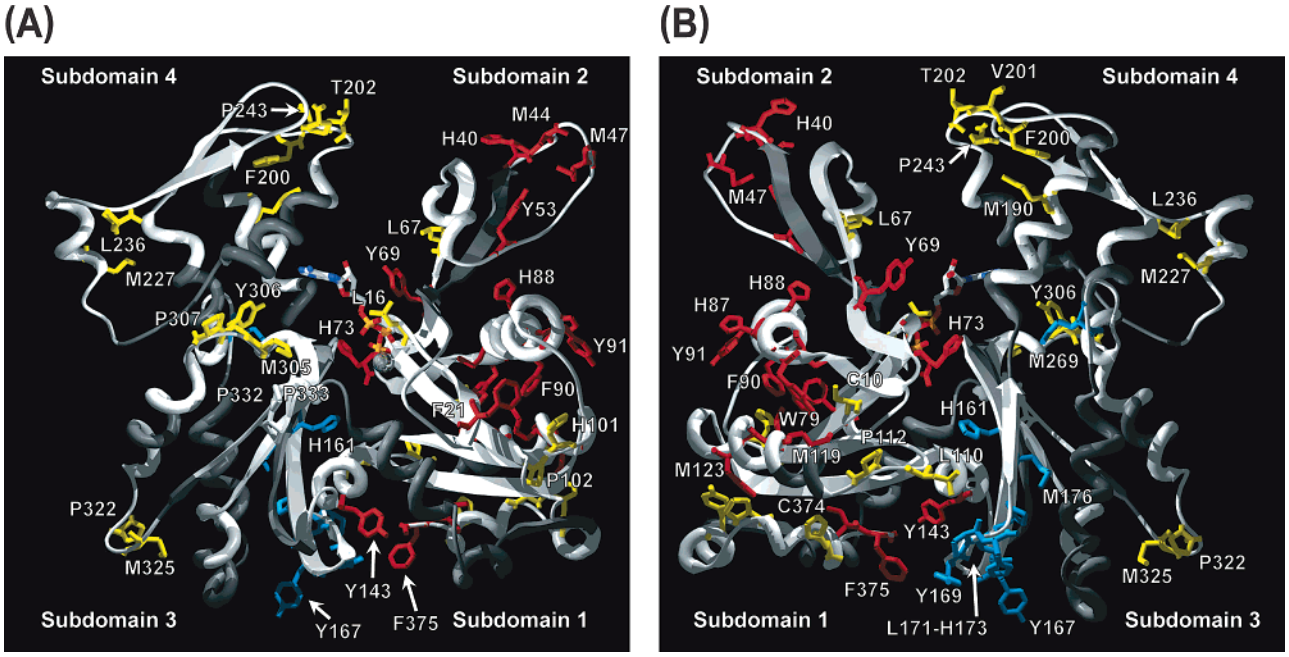

FIGURE 5: Protection sites observed in Mg-KCl-F-actin. Same coding as in Figure 4. A significant increase in protection is seen by the dominant red-colored residues in the figure.

119, and Met-123, show oligomerization-dependent protection; the oxidation rates of these residues were divalent-cation-independent in our previous studies. Peptide 363−375, which showed Mg-dependent protections in our previous work, also shows oligomerization-dependent protections. However, because peptide 360−372 shows no significant changes, we conclude that the protection is localized to Cys-374 and Phe-375 at the very C terminus.

KCl Increases the Extent and Range of Observed Protections. Mg filaments generated in the presence of KCl exhibit significant decreases in reactivity for many side chains compared to those generated in the absence of KCl. These changes occur in the absence of any visible changes in filament ultra-structure (Figure 3). The results are illustrated in Table 2 and on the structure of the actin monomer in Figure 5. The data of Figure 5 include side chains colored yellow that experienced modest protections of 1.3−2.9-fold compared to the Mg monomer as well as those showing robust filament-dependent protections (≥3.0) colored in red.

Multiple side-chain residues in and adjacent to the cleft between subdomains 2 and 4 show significant reactivity changes upon addition of KCl. Tyr-69 shows decreased reactivity upon filament formation, but the extent of protection for this residue is increased in the presence of KCl (Figure 5, red). Peptide 40−50, which contains the probe residues His-40, Met-44, and Met-47 (Figure 5, red), experienced a 10-fold protection upon filament formation in KCl. On the subdomain 4 side of the cleft, Pro-243 shows protection only in the presence of KCl (but only when peptide 239−254 is examined) (Figure 5, red), while the side chains from Phe-200 to Thr-202 show modest KCl-dependent protection. However, it should be noted that the reactive residues within this peptide are significantly buried in the Mg monomer.

Dramatic protections within subdomain 1 are seen as a function of KCl-dependent filament formation. For example, the reactivity of side chains Met-119, Met-123, and Phe-124 within peptide 118−125 (Glu-C digest) is reduced 8-fold in KCl compared with a 2-fold protection in the absence of KCl (Figure 5). Similar changes are seen in the overlapping peptide 119−147 from the trypsin digest, which experienced a 2−3-fold protection upon oligomerization in the absence of KCl and a greater than 10-fold protection in the presence of KCl (Figure 5). Phe-21 (seen within peptides 19−28 and 11−23) was protected 3-fold in the absence of KCl; it was further protected in the presence of KCl. The protection for peptides 360−372 and 363−375 increased in the presence of KCl as well. Because the former peptide exhibited no protection upon filament formation in the absence of KCl and both peptides had 2-fold increases in protection in the presence of KCl, it appears that the additional KCl-dependent protection is localized within residues 363−372, particularly Tyr-362, Pro-367, or His-371. Other segments within subdomain 1 exhibit protection for the Mg filament only in the presence of KCl; for example, compared to Mg monomers, we observe an 8-fold protection for peptide 85−95 (trypsin digest) confirmed by a 4-fold protection for peptide 84−93 (Asp-N). The protected residues within this peptide include His-87, His-88, Phe-90, and Tyr-91 (Figure 5, red). Of the two peptides that exhibited oligomerization-dependent increases in reactivity in the absence of KCl, one (residues 157−178) increased its rate of oxidation upon KCl addition, while Met-269, located in peptide 260−270, showed no further changes upon KCl formation (Figure 5, blue).

DISCUSSION

KCl Is Required to Generate Robust Interprotomer Contacts in the Actin Filament. Although the Mg^{2+}-ATP filament (in the absence of KCl) shows numerous protections relative to monomers indicative of filament assembly, the overall extents of protection are modest. For example, only peptides 19−28 and 11−23, for which Phe-21 is the probe side chain, have filament-dependent decreases in reactivity that approach 3-fold. Overall, for the 16 tryptic peptides analyzed in Table 2, 10 showed protections upon formation of filaments in the absence of KCl; these protections averaged 1.8-fold. Previous hydroxyl radical-mediated footprinting experiments have shown that, in the formation of a macromolecular interface, the resulting complex experiences decreases in reactivity for the solvent-accessible residues that are buried in the interface of at least 4-fold and often greater (*15*, *20*, *21*, *30*). Even the most robust protections observed for this filament preparation fall short of this standard. There are multiple possibilities that could give rise to these results. Because footprinting measures the ensemble average properties, dynamic conformational fluctuations or multiple states are observed as the time average or weighted average of the involved states sampled during the millisecond exposure time (*31*, *32*). Incomplete formation of filaments could give rise to the modest protections observed; however, both DLS and EM show a filamentous preparation (see Figures 2 and 3). The other possibilities are that the filaments are inhomogeneously packed, e.g., irregular, or that the contact regions are engaged in dynamic equilibrium fluctuations. Support for the latter explanation is seen with respect to the reactivity of peptides 363−375 and the partially overlapping peptide 360−372. The former peptide shows a 2.8-fold protection upon filament formation (absence of KCl), while the latter shows no changes. Thus, we can be sure that the structural changes are localized to Cys-374 and Phe-375. However, the ability of Cys-374 to react with sulfhydryl reactive reagents is maintained in actin filaments (*33*, *34*), which does not seem to be consistent with protection of the C terminus suggested by footprinting data. A likely explanation is that the filament (in the absence of KCl) experiences dynamic fluctuations of its interprotomer contacts, such that, on the time scale of cysteine-labeling experiments, all molecules have an opportunity to react with the derivitization reagent. On the much faster time scale of footprinting experiments, the weighted average of the populated states are sampled.

In contrast to what is observed in the absence of KCl, the data in the presence of KCl show extensive and robust protections. For filamentous actin in KCl, 15 of the 16 tryptic peptides showed protections that averaged 4.6-fold. In Figure 5, peptides exhibiting the most extensive burial are indicated in red. The side-chain probes within these peptides are more likely to be forming homogeneous macromolecular contacts (e.g., regular or the same everywhere) within the filament structure than is the case in the absence of KCl. Previous studies have indicated that KCl induces structural changes in actin filaments. The X-ray fiber diffraction data have suggested the effective diameter of the filament decreases in solution as the salt (NaCl) concentration is increased from 30 to 90 mM; however, the observed filaments in this study as analyzed by EM show no major changes in diameter (*35*, *36*). Polymerization of actin by increasing the ionic strength leads to a quenching of almost all ^{1}H NMR signals; however, distinct signals with relatively small line widths can still be observed in actin filaments, indicating the existence of mobile, NMR-visible residues in the macromolecular structure. These signals are quenched as ionic strength is increased further, indicating the loss of mobility of these residues, consistent with enhanced sequestration of side chains from the solvent, perhaps as a consequence of increased burial at interfaces (*37*). Thus, the KCl filament is more stable, and the dynamics of interprotomer interfaces (as detected by side-chain reactivities) are suppressed compared to the filament in the absence of KCl.

Longitudinal Contacts of the Helical Model of Actin Consistent with Footprinting Data. The helical model of actin makes specific predictions with respect to the intermolecular contacts of actin monomers in the filament (*12*). Using the

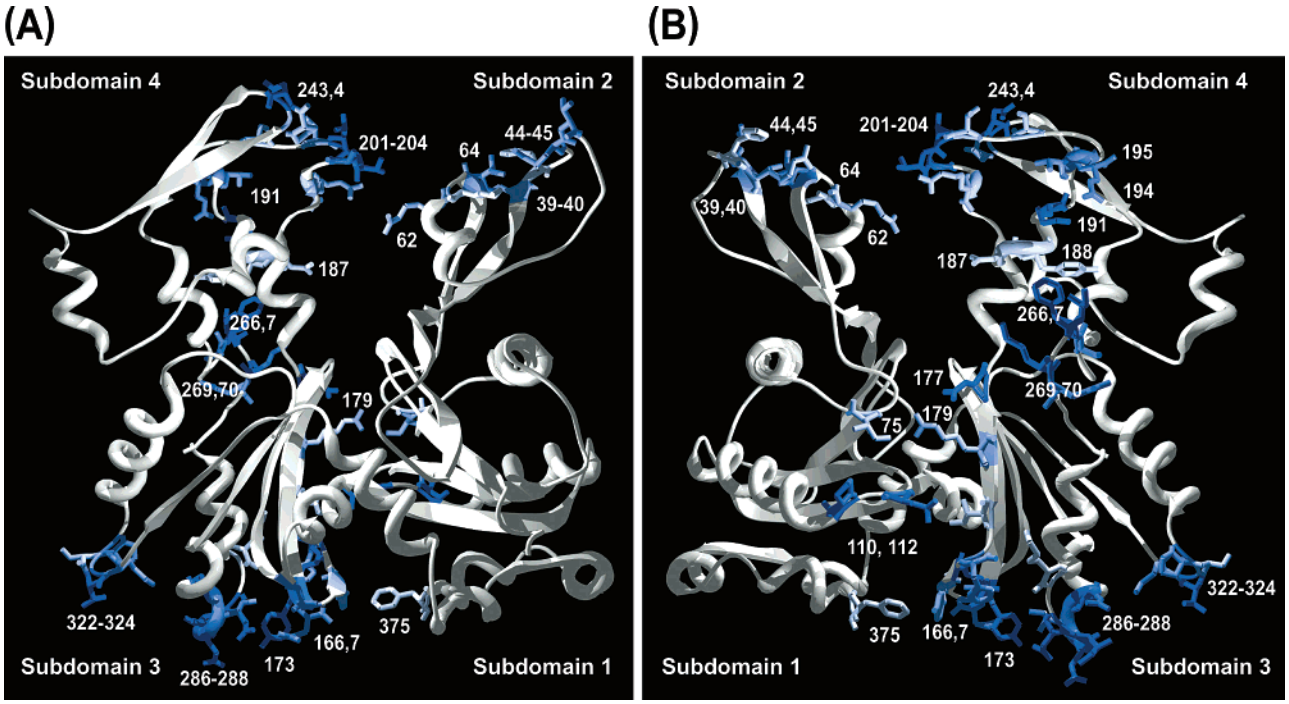

FIGURE 6: Calculated ASA changes upon the formation of F actin. The residues that are expected to be protected upon the formation of the Holmes model, F actin, are colored from white (no change) to blue (100% burial).

helical model of actin (Figure 1), we carried out surface-accessibility calculations on the side chains of individual monomer units compared to the packing of the same side chains in the filament (see the Experimental Procedures). One monomer of the five monomer unit, essentially the one in the middle of the helical stack, experiences the contacts representative of monomer units in a filament. On the basis of these calculations, Figure 6 illustrates the side-chain residues within actin that are predicted to experience protections based on the helical model of actin. These data are visualized as follows. The backbone segments whose side-chain residues are unprotected upon filament formation are shown in white, and the side chains that experience protection are explicitly drawn in blue with increasingly dark shades of blue for side chains that experience increasing burial.

A comparison of the footprinting data with the results indicated in Figure 6 provides remarkable agreement. In the examination of subdomain 2, the calculations indicate significant filament-dependent decreases in solvent-ASAs for Arg-39, His-40, Met-44, and Val-45; footprinting indicates that His-40, Met-44, and Met-47 (from tryptic peptide 40−50) are protected in the KCl filament. The helical model also predicts protections for Arg-62 and Ile-64; we see protections for adjacent residues Leu-67 and Tyr-69 from peptides 63−68 (trypsin) and 58−72 (Asp-N). Thus, the major contacts of subdomain 2 predicted by the helical model are consistent with the footprinting data observed for the KCl filament.

Within subdomain 4, footprinting data showing burial of Pro-243 are consistent with the specific predictions of the helical model. However, this protection is only seen for the tryptic peptide containing this residue in the presence of KCl. The model also predicts protections for residues 201−204. This is consistent with the decreased reactivity of the probe residues in peptide 197−206. However, this protection is only seen for the KCl form; protections for Pro-204 as well as for residues 201−204 might have been expected in the filament even in the absence of KCl. It may be that this state of the filament is sufficiently dynamic such that such protections are difficult to observe. Last, in subdomain 4, residues 191 and 195 are slightly buried in the helical model and peptide 184−191, where Met-190 is the primary probe, is seen to be protected in footprinting data of the KCl filament.

Within subdomain 3, the model predicts protections within residues 322−325. Footprinting data from peptide 316−326, where the primary probes are Pro-322 and Met-325, support this prediction. The model predicts burial of residues 286−288; a peptide with overlap in this region is not observed in our LC−MS experiments. The model also predicts a protection at the C terminus at residue 375; the footprinting data indicates that Cys-374 and Phe-375 are protected in the filament.

Filament-Dependent Enhancements of Side-Chain Reactivity. Although the footprinting data provide strong support for the overall framework of the helical model, some significant exceptions are seen. Within subdomain 4, the model predicts a significant protection of residues 265−270. However, the reactivity of peptide 260−270 is 5-fold enhanced in the filament. The source of the predicted filament-dependent protection is a lateral contact of residues 264−274, called the hydrophobic plug (H plug), within the filament architecture. In the modeling of the actin filament, this H plug was essentially "released" from contact with the actin monomer surface so that it could provide this lateral contact (*12*). For example, the surface accessibility of Phe-266, Ile-267, and Met-269 in the 1ATN crystal structure is $^1/_2$−$^1/_3$ of that seen for the actin protomer used for modeling the filament structure (see the Experimental Procedures). The reactivity of Met-269 in peptide 260−270 observed for the actin monomer (Table 1) is consistent with the 1ATN structure where the H plug is, overall, slightly accessible.

Deuterium-exchange MS data have also been used to examine the structure of F actin (*25*). Two peptides were examined that overlap with the H plug, including peptides containing residues 256−268 and 269−285. These data showed no change in reactivity of the backbone (within reported errors) for these two peptides when Ca-ATP-G-actin and Ca-ATP-KCl-F-actin species were compared. However, the Holmes model predicts a significant burial for these peptide segments compared to the solvent accessibility indicated for the backbone upon examination of the 1ATN structure. Mutagenesis has shown that actin forms with mutations at Val-266 and Leu-267 (Gly substitutions) are unable to polymerize (*38*), indicating a potential role for the H plug in mediating filament formation. Further, locking the H plug to the G-actin surface through disulfide bridges prevents actin polymerization as well (*39*, *40*). The latter experiment indicates, at the very least, that the H plug detaches from the monomer surface as part of the filament-assembly process. It is interesting that the footprinting data is consistent with such a detachment for the filament in the absence and presence of KCl. Overall, these results suggest that the role of the H plug in mediating filament assembly needs to be better defined.

Both the deuterium-exchange MS data and the footprinting data of this study indicate that segments of subdomain 3 experience significant increases in solvent accessibility that are not anticipated by an examination of the Holmes model. For example, peptide 156−170 in the deuterium-exchange MS experiments shows significant enhancement of deuteration upon filament formation. Footprinting data are quite consistent with this conclusion, as overlapping peptide 157−178 shows a 3-fold enhancement in reactivity in the KCl filament compared to the monomer data. Chik and Schriemer (*25*) have suggested that this may indicate conformational changes of the phosphate-binding loops that may mediate phosphate release in the filament. The deuterium-exchange MS data also indicate that backbone segments 11−18 show enhanced reactivity in the filament; this is suggested to be related to changes in specific interactions with the nucleotide phosphates as well. Our footprinting data from peptide 1−18 show filament-dependent protection of the side chains of Cys-10 and Leu-16; thus, potentially complex and likely interesting filament-dependent conformational changes occur at the N terminus of actin.

The side-chain reactivity information reported in this study of the actin filament is seen to provide conspicuous support for the helical model of the actin structure, particularly the longitudinal contacts between subdomains 3 and 4 and subdomains 1 and 2. The data also provide clues as to the dynamic nature of contacts that are possible in assembled filaments, depending on solution conditions. This is most clearly demonstrated in the case of the robust protections for the KCl filament state for peptides composed of residues 19−28, 40−50, 118−125, and 119−147. The D loop is well-known to experience multiple conformational states as a function of solution conditions; the finding that additional specific segments of the filament may vary in their dynamic fluctuations as a function of solution conditions is of great interest in understanding filament assembly and disassembly processes in the cell.

This work also provides direct comparison of results derived from deuterium-exchange MS and synchrotron-radiolysis MS experiments; the conclusions drawn are very similar. However, a perfect correspondence should not necessarily be expected because Ca-ATP-KCl filaments were examined in the deuterium MS study, while the Mg-ATP-KCl form is examined here. In addition, the techniques probe different structural elements; the backbone is probed for deuterium exchange versus side chains for footprinting. Nevertheless, it is clear that both approaches will be valuable in further defining the structure and dynamics of actin-filament assembly and the interactions of actin in its macromolecular complexes.

ACKNOWLEDGMENT

We are grateful to Frank Macaluso, Director of the Analytical Imaging Facility at the Albert Einstein College of Medicine, for his assistance and advice with the EM data of this paper.

REFERENCES

1. Pollard, T. D., Blanchoin, L., and Mullins, R. D. (2001) Actin dynamics, *J. Cell Sci. 114*, 3−4.
2. Pollard, T. D., Blanchoin, L., and Mullins, R. D. (2000) Molecular mechanisms controlling actin filament dynamics in nonmuscle cells, *Annu. Rev. Biophys. Biomol. Struct. 29*, 545−576.
3. Chen, H., Bernstein, B. W., and Bamburg, J. R. (2000) Regulating actin-filament dynamics *in vivo*, *Trends Biochem. Sci. 25*, 19−23.
4. Otterbein, L. R., Graceffa, P., and Dominguez, R. (2001) The crystal structure of uncomplexed actin in the ADP state, *Science 293*, 708−711.
5. Graceffa, P., and Dominguez, R. (2003) Crystal structure of monomeric actin in the ATP state. Structural basis of nucleotide-dependent actin dynamics, *J. Biol. Chem. 278*, 34172−34180.
6. Kabsch, W., Mannherz, H. G., Suck, D., Pai, E. F., and Holmes, K. C. (1990) Atomic structure of the actin:DNase I complex, *Nature 347*, 37−44.
7. Kabsch, W., and Holmes, K. C. (1995) The actin fold, *FASEB J. 9*, 167−174.
8. Schutt, C. E., Myslik, J. C., Rozycki, M. D., Goonesekere, N. C. W., and Lindberg, U. (1993) The structure of crystalline profilin: *β*-Actin. *Nature 365*, 810−816.
9. McLaughlin, P. J., Gooch, J. T., Mannherz, H. G., and Weeds, A, G, (1993) Structure of gelsolin segment 1-actin complex and the mechanism of filament severing, *Nature 364*, 685−692.
10. Otterbein, L. R., Cosio, C., Graceffa, P., and Dominguez, R. (2002) Crystal structures of the vitamin D-binding protein and its complex with actin: structural basis of the actin-scavenger system, *Proc. Natl. Acad. Sci. U.S.A. 99*, 8003−8008.
11. Vorobiev, S., Strokopytov, B., Drubin, D. G., Frieden, C., Ono, S., Condeelis, J., Rubenstein, P. A., and Almo, S. C. (2003) The structure of nonvertebrate actin: Implications for the ATP hydrolytic mechanism, *Proc. Natl. Acad. Sci. U.S.A. 100*, 5760−5765.
12. Holmes, K. C., Popp, D., Gebhard, W., and Kabsch, W. (1990) Atomic model of the actin filament, *Nature 347*, 44−49.
13. Lorenz, M., Popp, D., and Holmes, K. C. (1993) Refinement of the F-actin model against X-ray fiber diffraction data by the use of a directed mutation algorithm, *J. Mol. Biol. 234*, 826−836.
14. Pollard, T. D., and Cooper, J. A. (1986) Actin and actin-binding proteins. A critical evaluation of mechanisms and functions, *Annu. Rev. Biochem. 55*, 987−1035.
15. Guan, J. Q., Almo, S., and Chance, M. R. (2004) Synchrotron radiolysis and mass spectrometry: A new approach to research on the actin cytoskeleton, *Acc. Chem. Res. 37*, 221−229.
16. Guan, J. Q., Almo, S. C., Reisler, E., and Chance, M. R. (2003) Structural reorganization of proteins revealed by radiolysis and mass spectrometry: G-actin solution structure is divalent cation dependent, *Biochemistry 42*, 11992−12000.
17. Kiselar, J. G., Maleknia, S. D., Sullivan, M., Downard, K. M., and Chance, M. R. (2002) Hydroxyl radical probe of protein surfaces using synchrotron X-ray radiolysis and mass spectrometry, *Int. J. Radiat. Biol. 78*, 101−114.

18. Kiselar, J. G., Janmey, P. A., Almo, S. C., and Chance, M. R. (2003) Structural analysis of gelsolin using synchrotron protein footprinting, *Mol. Cell. Proteomics 2*, 1120−1132.
19. Kiselar, J. G., Janmey, P. A., Almo, S. C., and Chance, M. R. (2003) Visualizing the Ca^{2+}-dependent activation of gelsolin by using synchrotron footprinting, *Proc. Natl. Acad. Sci. U.S.A. 100*, 3942−3947.
20. Liu, R., Guan, J. Q., Zak, O., Aisen, P., and Chance, M. R. (2003) Structural reorganization of transferrin C-lobe and transferrin receptor upon complex formation: C-lobe to the receptor helical domain, *Biochemistry 42*, 12447−12454.
21. Guan, J. Q., Vorobiev, S., Almo, S. C., and Chance, M. R. (2002) Mapping the G-actin binding surface of cofilin using synchrotron protein footprinting, *Biochemistry 41*, 5765−5775.
22. Zhang, Z., and Smith, D. L. (1993) Determination of amide hydrogen exchange by mass spectrometry: A new tool for protein structure elucidation, *Protein Sci. 2*, 522−531.
23. Katta, V. and Chait, B. T. (1993) Hydrogen/deuterium exchange electrospray ionization mass spectrometry: A method for probing protein conformational changes in solution, *J. Am. Chem. Soc. 115*, 6317−6321.
24. Englander, S. W., and Kallenbach, N. R. (1983) Hydrogen exchange and structural dynamics of proteins and nucleic acids, *Q. Rev. Biophys. 16*, 521−655.
25. Chik, J. K., and Schriemer, D. C. (2003) Hydrogen/deuterium exchange mass spectrometry of actin in various biochemical contexts, *J. Mol. Biol. 334*, 373−385.
26. Spudich, J. A., and Watt, S. (1971) The regulation of rabbit skeletal muscle contraction. I. Biochemical studies of the interaction of the tropomyosin−troponin complex with actin and the proteolytic fragments of myosin, *J. Biol. Chem. 246*, 4866−4871.
27. Sclavi, B., Woodson, S., Sullivan, M., Chance, M. R., and Brenowitz, M. (1997) Time-resolved synchrotron X-ray "footprinting", a new approach to the study of nucleic acid structure and function: Application to protein−DNA interactions and RNA folding, *J. Mol. Biol. 266*, 144−159.
28. Ralston, C. Y., Sclavi, B., Sullivan, M., Deras, M. L., Woodson, S. A., Chance, M. R., and Brenowitz, M. (2000) Time-resolved synchrotron X-ray footprinting and its application to RNA folding, *Methods Enzymol. 317*, 353−368.
29. Maleknia, S. D., Ralston, C. Y., Brenowitz, M. D., Downard, K. M., and Chance, M. R. (2001) Determination of macromolecular folding and structure by synchrotron X-ray radiolysis techniques, *Anal. Biochem. 289*, 103−115.
30. Gupta, S., Mangel, W. F., McGrath, W. J., Perek J. L., Lee, D. W., Takamoto, K., and Chance, M. R. (2004) DNA binding provides a molecular strap activating the adenovirus proteinase, *Mol. Cell. Proteomics 3*, 950−959.
31. Ralston, C. Y., He, Q., Brenowitz, M., and Chance, M. R. (2000) Stability and cooperativity of individual tertiary contacts in RNA revealed through chemical denaturation, *Nat. Struct. Biol. 7*, 371−374.
32. Uchida, T., Takamoto, K., He, Q., Chance, M. R., and Brenowitz, M. (2003) Multiple monovalent ion-dependent patways for the folding of the L-21 *Tetrahymena thermophila* ribozyme, *J. Mol. Biol. 328*, 463−478.
33. Egelman, E. H., and Orlova, A. (1995) New insights into actin filament dynamics, *Curr. Opin. Struct. Biol. 5*, 172−180.
34. Orlova, A., and Egelman, E. H. (1995) Structural dynamics of F-actin: I. Changes in the C terminus, *J. Mol. Biol. 245*, 582−597.
35. Oda, T., Makino, K., Yamashita, I., Namba, K., and Maeda, Y. (1998) Effect of the length and effective diameter of F-actin on the filament orientation in liquid crystalline sols measured by X-ray fiber diffraction, *Biophys. J. 75*, 2672−2681.
36. Oda, T., Makino, K., Yamashita, I., Namba, K., and Maeda, Y. (2001) Distinct structural changes detected by X-ray fiber diffraction in stabilization of F-actin by lowing pH and increasing ionic strength, *Biophys. J. 80*, 841−851.
37. Slosarek, G., Heintz, D., and Kalbitzer, H. R. (1994) Mobile segments in rabbit skeletal muscle F-actin detected by ^{1}H nuclear magnetic resonance spectroscopy, *FEBS Lett. 351*, 405−410.
38. Kuang, B., and Rubenstein, P. A. (1997) Beryllium fluoride and phalloidin restore polymerizability of a mutant yeast actin (V266G, L267G) with severely decreased hydrophobicity in a subdomain 3/4 loop, *J. Biol. Chem. 272*, 1237−1247.
39. Shvetsov, A., Musib, R., Phillips, M., Rubenstein, P. A., and Reisler, E. (2002) Locking the hydrophobic loop 262−274 to G-actin surface by a disulfide bridge prevents filament formation, *Biochemistry 41*, 10787−10793.
40. Kim, E., Wriggers, W., Phillips, M., Kobabi, K., Rubenstein, P. A., and Reisler, E. (2000) Cross-linking constraints on F-actin structure, *J. Mol. Biol. 299*, 421−429.

BI048021J